THE JOURNAL OF BIOLOGICAL CHEMISTRY VOL. 281, NO. 10, pp. 6581–6588, March 10, 2006

Annular Arrangement and Collaborative Actions of Four Domains of Protein-disulfide Isomerase

*A SMALL ANGLE X-RAY SCATTERING STUDY IN SOLUTION**

Received for publication, August 1, 2005, and in revised form, December 28, 2005 Published, JBC Papers in Press, December 29, 2005, DOI 10.1074/jbc.M508422200

Sheng-jian Li[‡§1], Xin-guo Hong[¶1], Yuan-yuan Shi[‡§], Hui Li[‖], and Chih-chen Wang[‡2]

From the [‡]National Laboratory of Biomacromolecules and the [‖]Center for System Biology, Institute of Biophysics, Chinese Academy of Sciences, Beijing 100101, the [¶]Institute of High Energy Physics, Chinese Academy of Sciences, Beijing 100039, and the [§]Graduate School of the Chinese Academy of Sciences, Beijing 100049, China

We presented for the first time a small angle x-ray scattering study of intact protein-disulfide isomerase (PDI) in solution. The restored model revealed that PDI is a short and roughly elliptical cylinder with a molecular mass of 69 kDa and dimensions of 105 × 65 × 40 Å, and the four thioredoxin-fold domains in the order *a-b-b′-a′* are arranged in an annular fashion. Atomic force microscope imaging also supported the finding that PDI appears as an approximately flat elliptical cylinder. A PDI species with apparent molecular mass of 116 kDa measured by using size-exclusion chromatography, previously assumed to be a dimer, was determined to exist mainly as a monomer by using analytical ultracentrifugation. The C-terminal fragment 441–491 contributed to the anomalous molecular mass determination of PDI by size-exclusion chromatography. The annular model of PDI accounted for the cooperative properties of the four domains in both the isomerase and chaperone functions of PDI.

Protein-disulfide isomerase (PDI,[3] EC 5.3.4.1) is an abundant multifunctional protein within the lumen of the endoplasmic reticulum (1, 2). It plays important roles in many physiological processes as both an enzyme and a molecular chaperone (3–5) by assisting in folding, unfolding, and translocation of many disulfide-containing proteins (6) and even some disulfide-free proteins (7). In addition, PDI serves as an obligatory β subunit of hetero-oligomeric prolyl 4-hydroxylase (8) and microsomal triglyceride transfer protein (9) to maintain highly insoluble α subunits in an active, nonaggregated conformation (10).

The four-domain architecture of PDI in the order *a-b-b′-a′* was proposed when the PDI cDNA was first sequenced, according to the internal sequence homology within the molecule (11). Later, the domain boundaries were defined (12) and further refined as shown in Scheme 1 by combined use of protein engineering, limited proteolysis, and bioinformatics (13–16). The *a* and *a′* domains, each with a -CGHC- motif as the active site, share 47% sequence identity, whereas the *b* and *b′* domains, with no such active site motif, share 28% sequence identity (11). The C-terminal 29 residues, 463–491, constitute an acidic *c* extension (2), in which over half of the residues are Glu/Asp, and represent a putative Ca^{2+}-binding region (12). The three-dimensional structure determined by using NMR of the *a* domain, which shares 27% identity to thiroredoxin (Trx), shows a Trx-fold (15), and the *b* domain, which shows no significant sequence similarity to the *a* and Trx, also has a Trx-fold (14). PDI has thus been suggested to consist of four Trx-fold domains (14). Recently, a 19-amino acid linker region, 333–351, was identified between the *b′* and *a′* domains (16), which was suggested to potentially allow more flexibility between these domains than between the other domains. The three-dimensional structure of the entire PDI molecule, or of any other catalytically active eukaryotic PDI family member, has not yet been determined even though PDI was discovered over 40 years ago.

PDI had long been considered to be a homodimeric molecule according to its molecular mass determined by size-exclusion chromatography (SEC) (17, 18). Recently, by using analytical ultracentrifugation, it was reported that the dimeric 108-kDa species of PDI on SEC is actually a monomer, and PDI is a quite elongated molecule with an axial ratio of 5.7 (19). It was further suggested that the four reasonably globular Trx-fold domains are arranged in a linear fashion, and the anomalous molecular mass of PDI determined by SEC was ascribed to the elongated shape of the molecule.

By cross-linking with homo-bifunctional alkylating agents of different lengths, the minimum distance between the two active-site reactive groups, separately located in the *a* and *a′* domain, was determined to be only 16 Å (20). Many experimental data have shown that all four domains are required for PDI to exhibit the maximum catalytic activity (21) and perform chaperone activity efficiently (22). In contrast, the linear model would mean that there are few interactions between the domains. There are obvious contradictions in the molecular models of PDI in the published literature.

Small angle x-ray scattering (SAXS) has recently been proven to be a powerful tool for investigating the solution structure of biomacromolecules. This is partially due to a significant improvement in the *ab initio* methods for restoring the three-dimensional shape of a molecule from the observed one-dimensional scattering profile in a model-independent manner (23–26), *i.e.* no detailed structural data, such as crystal structure coordinates, are required.

Here we report, for the first time, the determination of the low resolution structure of the entire PDI molecule in solution using the SAXS technique with an *ab initio* shape-determination program, DAMMIN (25). The results indicate that the PDI molecule appears as a short and roughly elliptical cylinder, and its four Trx-fold domains are arranged in an annular and not a linear fashion. Examination of the SEC and/or

* This work was supported by Grants 2004CB520801 and 2006CB500703 from the Chinese Ministry of Science and Technology, Grants KSCX2-SW214-2 and KJCX2-SW-N06 from the Chinese Academy of Sciences, and Grant 10375075 from the Chinese Natural Science Foundation. The costs of publication of this article were defrayed in part by the payment of page charges. This article must therefore be hereby marked "*advertisement*" in accordance with 18 U.S.C. Section 1734 solely to indicate this fact.

[1] Both authors contributed equally to this work.

[2] To whom correspondence should be addressed: National Laboratory of Biomacromolecules, Institute of Biophysics, Chinese Academy of Sciences, 15 Datun Rd., Beijing 100101, China. Tel.: 86-10-64888502; Fax: 86-10-64872026; E-mail: chihwang@sun5.ibp.ac.cn.

[3] The abbreviations used are: PDI, protein-disulfide isomerase; Trx, *E. coli* thioredoxin; SEC, size-exclusion chromatography; SAXS, small angle x-ray scattering; AFM, atomic force microscope; Syn, α-synuclein; Trx-PDI (441–491), Trx with the fragment 441–491 of PDI fused to the C terminus; Trx-Syn (99–140), Trx with the fragment 99–140 of Syn fused to the C terminus; DTT, dithiothreitol; PDB, Protein Data Bank.

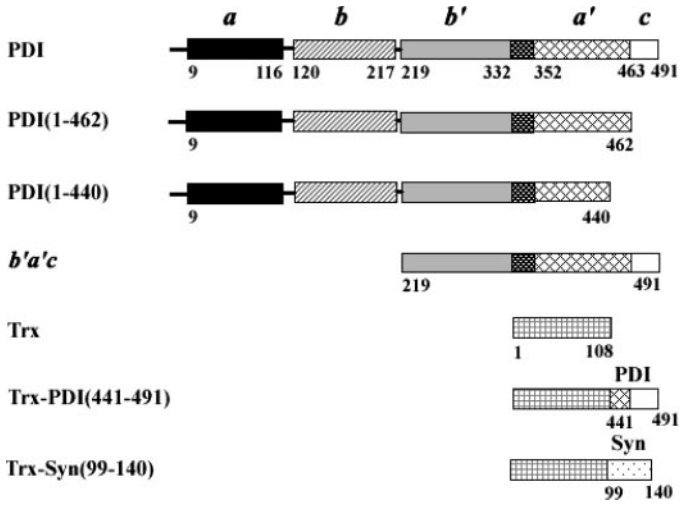

SCHEME 1. **Schematic domain structure of PDI, PDI mutants, and Trx chimeras.** The domain boundaries of PDI are based on Darby *et al.* (13), Kemmink *et al.* (14, 15), and Pirneskoski *et al.* (16).

analytical ultracentrifugation behavior of intact PDI, several C-terminally truncated variants, and Trx chimeras suggests that the C-terminal 441–491 fragment of PDI contributes to the discrepancy in molecular mass determinations as determined using these two techniques.

EXPERIMENTAL PROCEDURES

Protein Preparations—The plasmid pUC19-PDI, containing the full-length human PDI cDNA, was constructed from pBR322-PDI, a generous gift from Prof. K. Kivirikko, University of Oulu, Finland. The coding sequences of PDI and PDI mutants (Scheme 1) were amplified using pUC19-PDI as a template, and the PCR products with BamHI/HindIII sites were ligated into pQE30 to construct the corresponding expression plasmids. The plasmids of pQE30-Trx-PDI (441–491) and pQE30-Trx (with the additional 11 residues EFPGRPAAKLN at the C terminus of Trx) were constructed as described (22). By taking pQE30-Trx and pQE60-Syn (a plasmid containing the cDNA of α-synuclein (Syn) constructed by G. P. Ren of this group) as templates, the coding sequence of Trx-Syn (99–140) was constructed by overlap extension PCR, and the gene fusion digested with SacI/HindIII was then ligated into pQE30. The sequences of the constructs were verified by diagnostic PCR and DNA sequencing. All the constructs contain an N-terminal His tag (MRGSHHHHHHGS).

His-tagged proteins expressed in *Escherichia coli* M15 [REP4] were purified by using a nickel-nitrilotriacetic acid column (Amersham Biosciences) and were further purified using a Q-Sepharose Fast Flow column (Amersham Biosciences) eluted by using 50 mM Tris-HCl, pH 8.0 (hereafter referred to as Tris buffer), with a gradient of 0–1 M NaCl. Eluted fractions were examined by SDS-12% PAGE and pooled. For SEC, the proteins were buffer-exchanged to Tris buffer containing 0.2 M NaCl. For SAXS determinations at low protein concentrations (0.83, 1.65, and 3.3 mg/ml), PDI eluted from the Q-Sepharose Fast Flow column was buffer-exchanged to Tris buffer after the best monodisperse condition was confirmed by SEC and stored at −80 °C. The frozen samples were thawed just before performing SAXS experiments. For SAXS determinations at high protein concentrations (7.5 and 10.0 mg/ml) and AFM imaging, PDI eluted from the Q-Sepharose Fast Flow column was dialyzed thoroughly against distilled water at 4 °C, lyophilized, and redissolved in Tris buffer just before the determinations. For analytical ultracentrifugation determinations, proteins eluted from the Q-Sepharose Fast Flow column were dialyzed thoroughly against distilled water at 4 °C, lyophilized, and further purified on a Superdex 75 HR 10/30 column eluted with Tris buffer containing 0.2 M NaCl. The sample of reduced Trx-Syn (99–140) was prepared by treatment with 10 mM DTT overnight and then elution with Tris buffer containing 0.2 M NaCl and 0.5 mM DTT. Protein concentrations were determined by the Bradford method with bovine serum albumin as a standard (27). PDI used in this work showed 2.0 free thiols as determined with 5,5′-dithiobis-(2-nitrobenzoic acid) (28).

SAXS Measurements—Synchrotron SAXS measurements of PDI were carried out at the beamline BL-10C of the Photon Factory (Tsukuba, Ibaraki, Japan) (29). The scattered signals were detected using a one-dimensional position-sensitive proportional counter with 512 channels. At a sample-to-detector distance of 1 m and an x-ray wavelength λ of 1.488 Å, the scattering vector q ($q = 4\pi\sin\theta/\lambda$, where 2θ is the scattering angle) ranged from 0.01 to 0.35 $Å^{-1}$, which was calibrated by using dried hen collagen as a standard oriented specimen.

Samples in Tris buffer without NaCl were encapsulated inside a cell sandwiched by two thin parallel quartz windows 1 mm apart with a volume of 70 μl. All the SAXS experiments were carried out in a sample holder maintained at 25.0 ± 0.1 °C. SAXS data of buffer and samples were collected alternately in the frames of 60–300 s to avoid radiation-induced protein damage. PDI concentrations from 0.83 to 10.0 mg/ml in Tris buffer were measured so as to obtain the scattering curves at infinite dilution.

The data reduction includes normalization of the one-dimensional scattered data to the intensity of the transmitted beam and subtraction of the background scattering of the buffer. All of the scattering curves were then standardized to a protein concentration of 1 mg/ml. The low angle data were extrapolated to infinite dilution and merged with the high angle data measured at high protein concentrations to yield final scattering curves.

Scattering Data Analysis—The scattering intensity $I(q,c)$, expressed by the Guinier equation (30), is shown in Equation 1 as a function of the scattering vector q and the protein concentration c.

$$I(q, c) = I(0, c)\exp\left(-\frac{R_g(c)^2 q^2}{3}\right) \qquad \text{(Eq. 1)}$$

Here $I(0,c)$ is the forward scattering intensity, and $R_g(c)$ is the apparent radius of gyration at finite concentration.

At low protein concentrations, $I(0,c)$ may be written as shown in Equation 2,

$$K_c/I(0, c) = 1/M_r + 2A_2c + K \qquad \text{(Eq. 2)}$$

where K_c is a constant determined by using a series of concentrations of bovine serum albumin as a reference protein with the known molecular mass of 67 kDa (31). M_r is the molecular weight of the protein and can be obtained by extrapolating $K_c/I(0,c)$ to infinite dilution. A_2 is the second virial coefficient resulting from interparticle interference effects and can discriminate between attracting and repulsing interactions. Repulsing interactions lead to positive values of A_2, and attracting interactions lead to negative values.

At the dilute limit, $R_g(c)$ is shown in Equation 3,

$$R_g(c)^2 = R_0^2 - B_{if}c + K \qquad \text{(Eq. 3)}$$

where R_0 is the radius of gyration at infinite dilution, and B_{if} is a parameter reflecting inter-solute force potential (32). The sign of B_{if} means the same as that of A_2 (30). The three parameters A_2, R_0, and B_{if} were calculated using Equations 2 and 3.

The pair-distance distribution function, $P(r)$, given by Equation 4,

$$P(r) = \frac{1}{2\pi^2}\int I(q)(qr)\sin(qr)dq \qquad \text{(Eq. 4)}$$

is a measure of the frequency of interatomic vector lengths within a protein molecule and can provide more information about the shape of the scattering particle.

Ab Initio Molecular Shape Determination—The overall shapes of the protein were restored from the experimental scattering data by DAMMIN (25). Starting with a sphere with a diameter equal to the maximum particle size filled by ~1000 densely packed small beads (dummy atoms), DAMMIN searches for the best dummy atom model by minimizing the discrepancy function, $f(X) = \chi^2 + \alpha P(X)$, between the calculated and experimental curves using a simulated annealing method. $\alpha P(X)$ is a looseness penalty with positive weight for $\alpha > 0$, and χ is the discrepancy between the experimental $I_{exp}(q_j)$ and the calculated $I_{calc}(q_j)$ curves as shown in Equation 5,

$$\chi^2 = \frac{1}{N-1}\sum_j \left(\frac{I_{exp}(q_j) - c_{scal}I_{calc}(q_j)}{\sigma(q_j)}\right)^2 \qquad \text{(Eq. 5)}$$

where N is the number of experimental points; c_{scal} is a scaling factor, and $\sigma(q_j)$ is the experimental error at the momentum transfer q_j. The method is to modify the coordinates of beads randomly, while always approaching the configurations that decrease the energy $f(X)$. Starting from a random string, simulated annealing was employed to find a compact configuration of beads minimizing the discrepancy. In this method, a constant was subtracted from the experimental data to ensure that the intensity decay follows Porod's law for homogeneous particles.

Atomic Force Microscopy—A 10-μl drop of PDI solution at 2.5 μg/ml in Tris buffer was deposited onto a piece of freshly cleaved mica, incubated at room temperature for 10 min, and then rinsed with Tris buffer to remove loosely bound protein. Imaging was performed using a NanoScope IIIa multimode AFM (Veeco Instruments, Santa Barbara, CA) with an E-scanner (10 μm × 10 μm) operating in tapping mode. The cantilevers (100 μm, NP-S, Veeco Instruments) were oscillated at a frequency of ~8 kHz, and the set point was regulated to have the minimum possible force exerted on the sample while maintaining the sharpness of the image. Height images were collected with a scan rate of 1 Hz.

Analytical Ultracentrifugation—Sedimentation experiments were performed using an XL-I analytical ultracentrifuge (Beckman Coulter) equipped with a four-cell An-60 Ti rotor at 20 °C. Tris buffer containing 0.2 M NaCl (plus 0.5 mM DTT in the case of reduced Trx-Syn (99–140)) was used as the reference solution.

Sedimentation velocity experiments were performed at a speed of 50,000 rpm for PDI and 60,000 rpm for other samples at a concentration of 0.75 mg/ml. Scans were taken at 280 nm with a radial step size of 0.003 cm. Differential sedimentation coefficients, $c(s)$, were calculated by least squares boundary modeling of sedimentation velocity data using SEDFIT (33) from www.analyticalultracentrifugation.com/download.htm. The values of apparent sedimentation coefficients were corrected to $s_{20,w}$ for solvent viscosity by using SEDNTERP from www.jphilo.mailway.com/download.htm. The frictional coefficients (f/f_0) and axial ratios (a/b) were calculated by using the vbar method in Sednterp, assuming a prolate ellipsoid model.

Sedimentation equilibrium experiments were performed at a speed of 20,000 rpm at protein concentrations of 0.2 and 0.3 mg/ml. Scans were taken at 280 nm with a radial step size of 0.001 cm. For each run, it was verified that equilibrium had been reached until there was no significant difference in scans taken 2 h apart. After the data at equilibrium had been collected, the rotor speed was increased to 40,000 rpm and run for a further 4 h to deplete the meniscus, so that the base line at the meniscus could be measured experimentally. The molecular mass was calculated using the Beckman data analysis software version 5.0 in which absorbance *versus* radial position data were fitted to the sedimentation equilibrium equation using a nonlinear least squares method. The resulting data sets were analyzed globally using the "self" or the "ideal single-species" model.

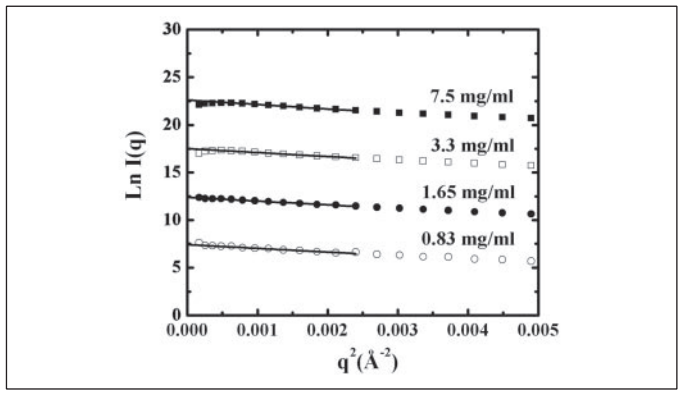

FIGURE 1. **Dependence of Guinier plots on concentrations of PDI.** The protein concentrations were as indicated. The *straight lines* were fitted to the data over the region of 8.0×10^{-4} to 2.5×10^{-3} (Å^{-2}) by the least squares method. For clarity, the plots have been arbitrarily shifted along the *y* axis.

RESULTS

SAXS Parameters—As shown in Fig. 1, the Guinier plots of the experimental SAXS data at all concentrations were linear in most of the low q region, indicating that PDI protein did not undergo aggregation. The slight downward curvature in the region with very low q near the direct beam stopper, possibly resulting from weak inter-particle interference, was alleviated with decreasing protein concentrations and was negligible for the dilute samples with concentrations of 1.65 and 0.83 mg/ml. To get accurate concentration dependence data and to avoid any influence of x-ray beam stability near the beam stopper, the straight lines were fitted by the least squares method to the measured data within the region 8.0×10^{-4} to 2.5×10^{-3} (Å^{-2}).

The function $K_c/I(0,c)$ evaluated from the intercepts of the Guinier plots was linear over the entire concentration range (Fig. 2*A*), and the slope, which represents the value of A_2, was $-(4.4 \pm 0.3) \times 10^{-4}$ ml mol g^{-2}. The square of apparent radius of gyration $R_g(c)$ calculated from the slopes of the Guinier plots also showed a linear relationship with protein concentration (Fig. 2*B*), and the slope, which represents the value of B_{if}, was $-(34.5 \pm 3.6) \times 10^{-13}$ cm^5 g^{-1}. The values of A_2 and B_{if} are both negative, indicating attractive interactions between the PDI molecules in solution. The molecular mass of PDI was determined to be 69 ± 3 kDa, indicating that PDI exists as a monomer in solution under the experimental conditions used. The radius of gyration at infinite dilution, *i.e.* R_g (0), was calculated to be 33.2 ± 0.3 Å.

The pair-distance distribution function $P(r)$ (Fig. 3) was obtained from the entire scattering curve $I(q)$ in the range of q, from zero to q_{max}, by direct Fourier transformation (Equation 4). In the low angle region ($q < 0.05$ Å^{-1}), $I(q)$ was extended to zero by using R_g (0). In the high angle region ($q > 0.05$ Å^{-1}), concentrated solutions were used to improve the statistics, as the scattering intensity is not affected by inter-particle interactions. The maximum linear dimension, D_{max}, determined from $P(r)$ is 105 ± 5 Å, and the radius of gyration estimated from

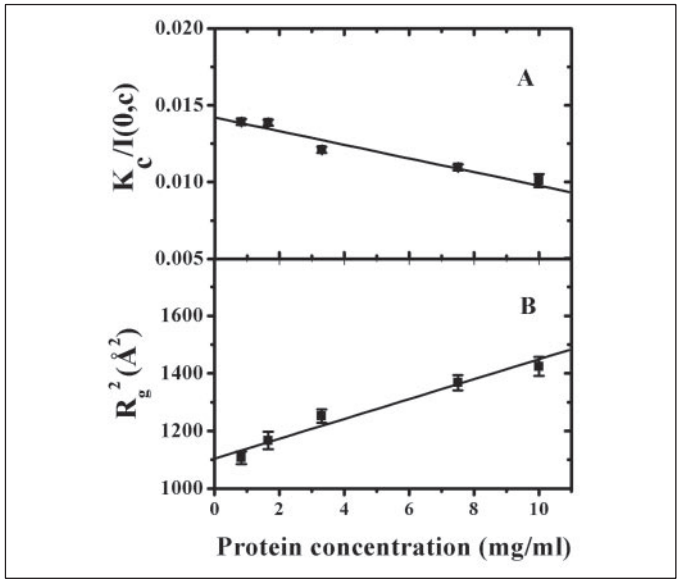

FIGURE 2. **Protein concentration dependence of $K_c/I(0,c)$ and $R_g(c)$ of PDI.** The values of $K_c/I(0,c)$ and $R_g(c)$ were calculated as described under "Experimental Procedures."

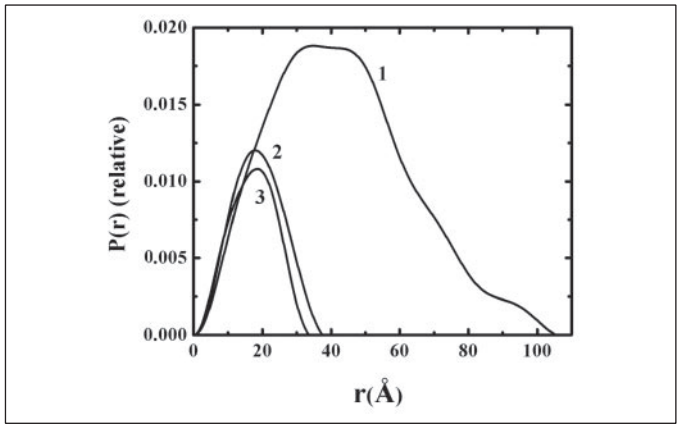

FIGURE 3. **Pair-distance distribution function *P(r)*.** The *P*(*r*) values for PDI (*curve 1*) were calculated from the experimental scattering curves using Equation 4 (see "Experimental Procedures"). The *P*(*r*) values for domain *a* (*curve 2*) and domain *b* (*curve 3*) were computed from the atomic models of the corresponding NMR structures by CRYSOL and GNOM.

the *P*(*r*) function by applying the GNOM package to the entire scattering profile, in the range 0.01 Å^{-1} to q_{max}, is 33.7 ± 0.3 Å, which is consistent with the corresponding value of 33.2 ± 0.3 Å estimated from the extrapolated Guinier plots.

The *P*(*r*) functions calculated from the three-dimensional coordinates (PDB code 1MEK) of domain *a* (sequence 1–120) and of domain *b* (PDB code 1BJX) (sequence 119–218) using CRYSOL and GNOM were compared with that of PDI (Fig. 3). The NMR structure of domain *b*, analyzed by Kemmink *et al.* (34), actually contains 10 amino acid residues (219–228) more than the currently identified *b* domain (Scheme 1). The structure of this extra part was found to be disordered and was thus deleted in the *P*(*r*) function calculation for the *b* domain. The value of D_{max} of 105 Å for PDI is much smaller than two times the sum of the corresponding values of 37 Å for the *a* domain and 33 Å for the *b* domain; therefore, the four domains are not arranged linearly, which would give a value of D_{max} larger than 140 Å.

Ab Initio Molecular Shape—Dummy atom modeling was performed from the scattering pattern up to q_{max} = 0.25 Å^{-1} using DAMMIN within a spherical search diameter of D_{max} = 105 Å without symmetrical constraint. The uniqueness and the stability of the restored shapes were checked by repeated modeling. Twenty independent models were then aligned and averaged using the programs SUPCOMB (35) and DAMAVER (36), which superimposed all models and determined the common envelope containing all models. In the next round, this common envelope was used as an initial search volume for all new models. Twenty runs of the *ab initio* shape determination produced consistent results, as all output models yielded nearly identical scattering patterns (Fig. 4, *solid line*) with a discrepancy of χ = 1.3 to the respective corrected experimental data obtained by subtracting a constant in the scattering range up to 0.25 Å^{-1}. These final models were again aligned and averaged using SUPCOMB and DAMAVER. The averaged dummy atom model at three orthogonal orientations (Fig. 5, *left column*) suggests a short and roughly elliptical cylinder with approximate dimensions of 105 × 65 × 40 Å. By using the three-dimensional structure visualization software RasTop, a shallow concave area with low electrical density was found in the center of the molecule. DAMSEL (part of the DAMAVER package) was employed to align all of the possible pairs of models and to identify the most probable model (Fig. 5, *right column*), which should yield the smallest average discrepancy. The result showed a molecule with very similar shape to that obtained by averaged dummy atom modeling (Fig. 5, *left column*) except that it had a significant small cavity of about 20 Å in diameter at the center. This cavity corresponds well to the shallow concave area in the averaged dummy atom model.

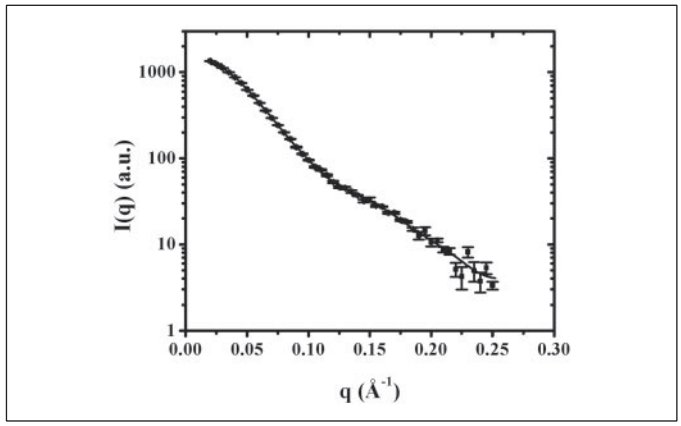

FIGURE 4. **X-ray scattering pattern of PDI in solution.** *Solid line*, scattering from the DAMMIN bead model. The scattering curve was standardized to that of a protein concentration of 1 mg/ml.

AFM Imaging—As shown in Fig. 6, most of the particles randomly distributed on a mica substrate do not show linear shape. By evaluation of the ratio of the full width at half-maximum height for the longest to that of the shortest size of a particle by the method of section analysis using Nanoscope version 6.12, the average ratio of 211 particles in several AFM images was calculated to be 1.26 ± 0.15. Allowing for the inevitable tip broadening of AFM imaging (37), PDI molecules in AFM image appeared as approximately flat elliptical cylinders.

Fragment 441–491 and the Abnormal Behavior of PDI on SEC—In contrast to the *a*, *b*, *b′*, and *a′* domains, the C-terminal sequence 463–491, *c*, has never been assigned as a structural domain but is just an extension (2), probably with no secondary or tertiary structure (38). We prepared several PDI mutants with the C-terminal sequence deleted to different extents in order to examine the behavior of these mutants by SEC.

PDI was found to elute at a position corresponding to an apparent molecular mass of 116 kDa (SEC profiles are not shown), and PDI (1–462) with the whole *c* extension deleted eluted as two peaks of 120 and 65 kDa. According to the calculated monomeric molecular mass of

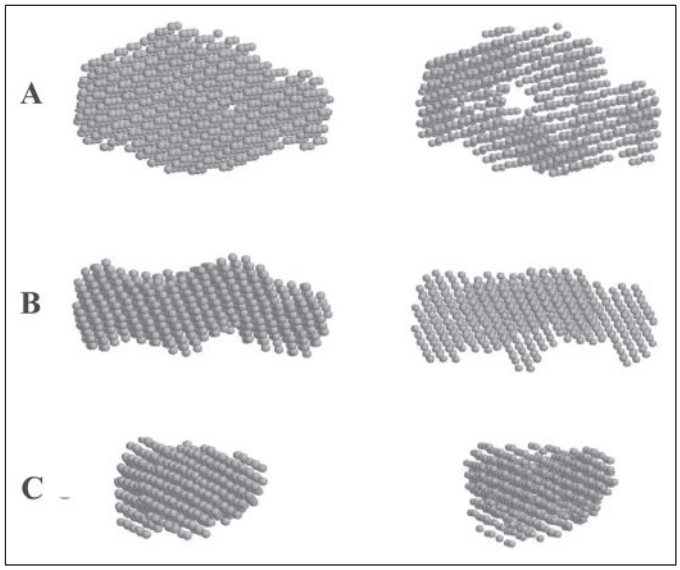

FIGURE 5. **Restored models of PDI.** *A*, *top view*; *B*, *front view*; and *C*, *side view*. *Left column*, the averaged model. *Right column*, the most probable model by DAMMIN using a q_{max} of 0.25 $Å^{-1}$ with no symmetrical constraint.

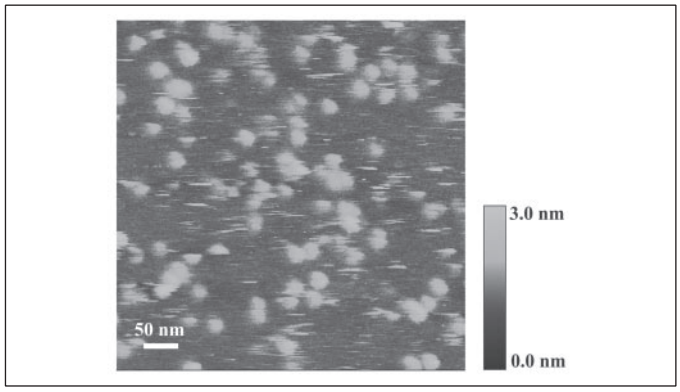

FIGURE 6. **AFM image of PDI in tapping mode.** Image size 500 × 500 nm, *z* range 0–3 nm.

56.719 kDa (the additional N-terminal His tag was included), PDI appears to be a homodimer, and PDI (1–462) is a mixture of dimers and monomers (Table 1). PDI (1–440), with a further 22 residues deleted and missing the last α-helix and a part of a loop in the *a′* domain (10, 16), eluted as a single peak of 60 kDa, a monomer. In addition, the C-terminal fragment *b′a′c*, which has a calculated monomeric molecular mass of 32.73 kDa, eluted as two peaks with apparent molecular masses of ~700 and 62 kDa on SEC and eluted as a single peak of 62 kDa after treatment with DTT, consistent with a dimer. The 700-kDa species is presumably a disulfide-bonded high order oligomer. Another C-terminal fragment 308–491 of PDI has also been reported to behave as a dimer on SEC (39). Therefore, it seemed to us that the species containing the C-terminal 441–491 sequence consistently elutes with an apparent molecular mass equivalent to a dimer on SEC, whereas PDI (1–440) behaves as a monomer.

Analytical ultracentrifugation was used to check the association state of PDI. As shown in Fig. 7*A*, the *c*(*s*) distribution indicated that the dimeric 116-kDa species of PDI on SEC sedimented as a major species with apparent sedimentation coefficient of 3.26 S. The *c*(*M*) distribution transformed from the *c*(*s*) distribution indicated that the molecular mass is 64 kDa (Table 1). The sedimentation equilibrium data were globally fitted to the self model for two initial loading concentrations, and a best fit (random residuals and low variance) was then acquired using a model containing monomer-dimer-tetramer, in which the molecular mass of the PDI monomer was set to 56.719 kDa (Fig. 8*A*). The dissociation constants for PDI monomer/dimer and dimer/tetramer were determined to be 9.9 and 15.4 μM, respectively. Taken together, the analytical ultracentrifugation results from this and previous work (19) indicated that the "dimeric" species of PDI observed by SEC is in fact mainly a monomer.

As PDI (19) and PDI (308–491) (39) have been characterized to be monomeric by analytical ultracentrifugation, and also by SAXS for PDI, the C-terminal 441–491 sequence is likely a contributor to the anomalous behavior of these molecules on SEC.

To examine this assumption, we further prepared two chimeric proteins, Trx-PDI (441–491) and Trx-Syn (99–140), in which the C-terminal 441–491 fragment of PDI and a C-terminal 99–140 fragment of natively unstructured Syn was fused to the C terminus of Trx, respectively (Scheme 1). Trx is a typically globular and compact molecule (PDB code 2TRX) with an axial ratio of ~1 and dimensions of 30 × 30 × 25 Å and showed a molecular mass of 13.8 kDa on SEC, which is very close to the calculated value of 14.3 kDa (Table 1). The chimera of Trx-PDI (441–491) eluted at a position corresponding to an apparent molecular mass of 40.4 kDa, corresponding to the size of a dimer. The C-terminal fragment 99–140 of Syn is similar to the *c* extension of PDI in terms of the acidity (14, 40) and the Ca^{2+} binding activity (12, 41) and has random coil configuration as determined by NMR (42). Trx-Syn (99–140) eluted on SEC as two peaks corresponding to tetramer (peak 1, 70.2 kDa) and dimer (peak 2, 35.0 kDa). After treatment with DTT, the reduced Trx-Syn (99–140) eluted as a single peak of 35.0 kDa corresponding to a dimer. The *c*(*s*) distributions of Trx-PDI (441–491), peak 1 of Trx-Syn (99–140) on SEC, and the reduced Trx-Syn (99–140) showed that they sedimented with apparent sedimentation coefficients of 1.66 S (Fig. 7*B*), 2.28 S (Fig. 7*C*), and 1.59 S (Fig. 7*D*), respectively (Table 1). The *c*(*M*) distribution corresponded to molecular masses of 22, 44, and 20 kDa, respectively. The sedimentation equilibrium data were globally fitted to the ideal single-species model for two initial loading concentrations, and the molecular masses calculated from the best fit (random residuals, low variance) are 19.1 kDa (Fig. 8*B*), 35.0 kDa (Fig. 8*C*), and 18.6 kDa (Fig. 8*D*), in agreement with the molecular masses *c*(*M*) calculated from sedimentation velocity (Table 1). The above results indicate that the apparently dimeric species of Trx-PDI (441–491) and Trx-Syn (99–140) observed by SEC are actually monomeric, and the apparently tetrameric species of Trx-Syn (99–140) observed by SEC is actually dimeric. It turns out that fusion of the PDI fragment 441–491 or the natively unstructured fragment 99–140 of Syn to a compactly structured Trx molecule converted the normal chromatography of Trx to one that is anomalous.

DISCUSSION

PDI Exists as a Short and Roughly Elliptical Cylinder—The low resolution structure of the entire PDI molecule in solution has been determined for the first time by using the SAXS technique. The restored averaged DAMMIN model shows that PDI is a short and roughly elliptical cylinder (Fig. 5). AFM image of PDI also showed an approximately flat elliptical cylinder. As PDI has been suggested to be composed of two active and two inactive Trx-fold domains (14), it is rational to superimpose the most probable model with the NMR structures of two *a* domains and two *b* domains in the order *a-b-b-a* (Fig. 9). The result showed that the four Trx-fold structures arranged in such an annular way were accommodated very well within the envelope of the restored model of entire PDI molecule. In addition, the annular arrangement of

TABLE 1
Parameters determined by SEC and analytical ultracentrifugation

Protein	M_{CAL}[a]	M_{SEC}[a]	Apparent association state	Sedimentation velocity					$M_{S.E.}$[a]	Association state
				S^b	$s_{20,w}$	f/f_0	a/b	M_{SV}[a]		
	kDa			*S*				*kDa*	*kDa*	
PDI	56.719	116 ± 3	Dimer	3.26	3.48	1.51	5.5	64		Monomer[c]
PDI (1–462)	53.342	120 ± 3	Dimer/monomer							
		65 ± 1								
PDI (1–440)	51.076	60 ± 1	Monomer	3.08	3.29	1.47	5.0	67		Monomer[c]
b′a′c	32.730	~700	Oligomer/dimer							
		62 ± 2								
b′a′c (reduced)[d]		62 ± 2	Dimer							
Trx	14.277	13.8 ± 0.8	Monomer	1.39	1.49	1.36	3.9	16		Monomer
Trx-PDI (441–491)	19.014	40.4 ± 1.0	Dimer	1.66	1.77	1.46	4.8	22	19.1	Monomer
Trx-Syn (99–140)	17.792	70.2 ± 1.0	Tetramer	2.28	2.44	1.60	6.8	44	35.0	Dimer
		35.0 ± 1.0	Dimer	1.59	1.70	1.44	4.6	20	18.6	Monomer
Trx-Syn (99–140) (reduced)[d]		35.0 ± 1.0	Dimer	1.59	1.70	1.44	4.6	20	18.6	Monomer

[a] M_{CAL} indicates calculated molecular mass. M_{SEC} indicates molecular mass determined by SEC. Chromatography of PDI, PDI (1–462), PDI (1–440), and *b′a′c* was performed on a Superdex 200 HR 10/30 column with molecular mass markers (Bio-Rad) as follows: bovine thyroglobulin, 670 kDa; bovine γ-globulin, 158 kDa; chicken ovalbumin, 44 kDa; equine myoglobin, 17 kDa; and vitamin B_{12}, 1.35 kDa. Chromatography of Trx, Trx-PDI (441–491), and Trx-Syn (99–140) was performed on a Superdex 75 HR 10/30 column with molecular mass markers (Amersham Biosciences) as follows: albumin, 67 kDa; ovalbumin, 43 kDa; chymotrypsinogen A, 25 kDa; ribonuclease A, 13.7 kDa. Elutions were performed at 0.5 ml/min in Tris buffer containing 0.2 M NaCl. Data are expressed as mean ± S.D. (n = 3–5). M_{SV} indicates molecular mass determined by sedimentation velocity, *i.e.* the ordinate maximum of each peak in the best fit $c(M)$ distribution (data not shown). $M_{S.E.}$ indicates weight-average molecular mass from sedimentation equilibrium analysis (Fig. 8).
[b] Apparent sedimentation coefficient, the ordinate maximum of each peak in the best fit $c(s)$ distribution (Fig. 7).
[c] According to the $c(s)$ distribution (Fig. 7), the dimeric species of PDI on SEC contained ~25% dimer, and the monomeric species of PDI (1–440) on SEC contained ~10% dimer.
[d] Treated with 10 mM DTT for 2 h at room temperature.

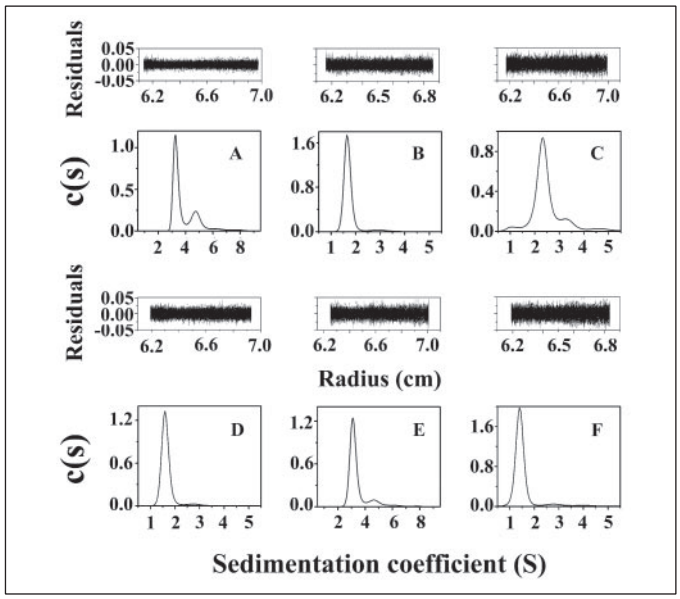

FIGURE 7. **Sedimentation coefficient distributions derived from sedimentation velocity profiles.** *A*, PDI; *B*, Trx-PDI (441–491); *C*, Trx-Syn (99–140) (peak 1 on SEC); *D*, reduced Trx-Syn (99–140); *E*, PDI (1–440); and *F*, Trx.

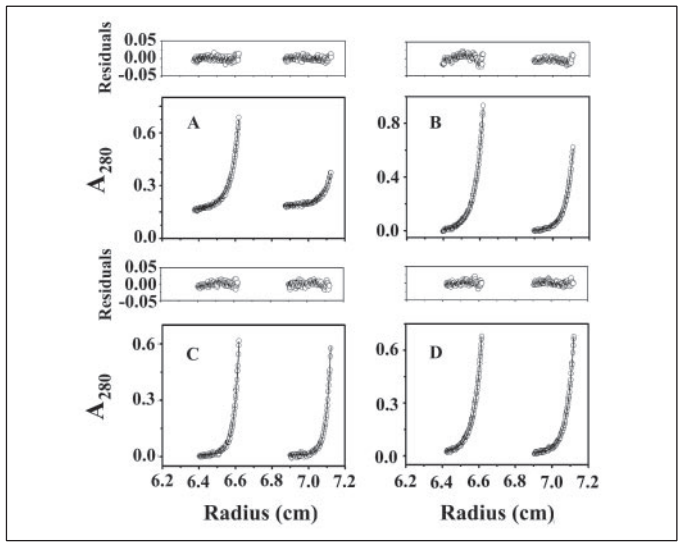

FIGURE 8. **Sedimentation equilibrium.** The absorbance at 280 nm was plotted *versus* radial distribution profiles fit globally by protein concentration. The *solid lines* represent the global nonlinear least squares best fits to the data at two protein concentrations of 0.3 (*left*) and 0.2 mg/ml (*right*) according to the "monomer-dimer-tetramer" model for PDI (*A*) and the ideal single-species model for Trx-PDI (441–491) (*B*), Trx-Syn (99–140) (peak 1 on SEC) (*C*), and reduced Trx-Syn (99–140) (*D*).

the four Trx-fold domains forms a small cavity in the center of the molecule, and this cavity appears to be a significant structure, because its location is fully consistent with that of the shallow concave area unambiguously identified in averaged models not only by DAMMIN but also by GASBOR (26). The GASBOR models are in fact very similar to those produced using DAMMIN but are not shown here because of unsatisfactory statistics in the x-ray scattering curves at high angles ($q > 0.25$ Å^{-1}). The *c* extension is not identified in the present restored models. As the resolution in the models constructed using SAXS is limited, and the NMR structures of the domain *a* and *b* were used to replace the structures of *a′* and *b′*, the restored model presented here is reasonable and very probable but does not necessarily represent a unique solution to modeling the data.

Many experimental data have shown that all four domains cooperate with each other to participate in binding of the protein target (22, 43, 44), although the *b′* domain contributes to the principal peptide-binding site (45). All four domains have been found to be required for PDI to perform efficiently as a chaperone (22, 43, 44) and to exhibit maximum catalytic activity (21). The isolated *a* or *a′* domain can catalyze simple reduction or oxidation reactions of disulfide bonds, but it is not able to catalyze complex isomerizations of proteins containing several disulfide bonds, as native PDI is able to do (46). The activity of full-length PDI is not simply the sum of the activities of the isolated *a* and *a′* domain. This suggests that other parts of the PDI molecule are required for its full range of activities. A binding site in the *a* domain has been found recently to contribute to prolyl 4-hydroxylase tetramer assembly (44), in addition to the *a′* and *b′* domains, which have been found to fulfill the minimum requirement for function of PDI as a subunit of prolyl 4-hydroxylase (43).

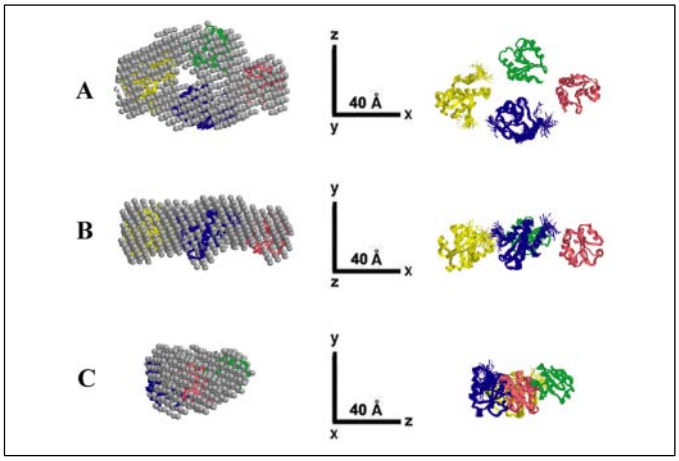

FIGURE 9. **The most probable model of PDI by DAMMIN superimposed with NMR structures of PDI domains.** *A*, *top view*; *B*, *front view*; and *C*, *side view*. *Left column*, the most probable model from the *right column* of Fig. 5 was superimposed with the NMR structures (shown in *right column*) of two *a* domains (PDB code 1MEK, *blue* and *yellow ribbons*) and two *b* domains (PDB code 1BJX with the 219–228 sequence deleted, *pink* and *green ribbons*) in the order *a*-*b*-*b*-*a*. In the counterclockwise arrangement of *a*-*b*-*b*′-*a*′ the *blue* denotes the domain *a*.

Based on a range of functional studies of PDI as published previously, the annular arrangement of *a*-*b*-*b*′-*a*′ in the counterclockwise way is preferred (Fig. 9). This model provides a good structural basis for the synergic function of PDI domains, allowing all four domains (especially *a*, *b*′, and *a*′) to cooperate with each other to form a site for binding and stabilizing a partially unfolded conformation of a protein substrate. Protein folding involving complex isomerization steps would require substantive conformational changes in the substrate as well as thiol-disulfide chemistry (1). The entire PDI molecule, with such an annular domain arrangement, can catalyze those protein folding reactions through cooperative action not only between the *a* and *a*′ domains but also involving the *b*′ domain, which does not participate directly in thiol-disulfide exchange, because of lack of a -C*XX*C- active site, but provides the principal specific peptide-binding site (1, 2). In the present model the *a* and *a*′ domains could be very close to each other, consistent with the cross-linking results (20), so that they can function synergistically; in contrast, the two domains would be at least 60 Å apart if the four domains were arranged in a linear fashion. Because the cavity observed in this model appears not to be sufficiently large to allow all possible PDI substrates to fit, the inter-domain motion is likely required for the full range of PDI activities. Recently the region (333–351) between the *b*′ and *a*′ domains has been identified to be a linker, which was suggested to potentially allow more flexibility between these two domains than between the other domains so large substrate binding would fit (16). Therefore, the annular structure of PDI should be viewed as a dynamic but not a static structure. In this respect, the hinged linker helix between the N- and the C-terminal domains of DsbC subunit is also long (16 residues), which has been suggested to provide sufficient flexibility to allow the binding of different sized substrates (47). Therefore, in assisting the folding of multidisulfide-containing proteins, PDI, with such a dynamic annular domain arrangement, is fully able to function as a chaperone, binding and stabilizing different sized folding intermediates by the *b*′ domain as a main site together with other domains around the cavity or the concave area. PDI can also function as an isomerase, catalyzing the formation of native disulfides by synergic actions of *a* and *a*′ domains located not far away.

Axial Ratio Calculation Using Analytical Ultracentrifugation—The linear model of PDI was based on an axial ratio of 5.7 calculated using sedimentation velocity data (19). Using SEDNTERP software on sedimentation velocity data, we got an axial ratio of 5.5 for the PDI monomer (Table 1), which is indeed very similar to 5.7. However, the axial ratio of Trx-PDI (441–491) and the monomeric Trx-Syn (99–140) were calculated to be 4.8 and 4.6, respectively, which are also similar to the value for PDI. The PDI molecule is composed of four successive Trx-fold domains and a *c* extension, but it is not an elongated molecule, whereas Trx-PDI (441–491) is composed of only one Trx-fold domain and a fragment of about 50 residues, which also exists in the PDI molecule. The PDI (1–440) monomer without the C-terminal 51 residues has a calculated axial ratio of 5.0, very close to the value of 5.5 for the entire PDI molecule (Fig. 7*E* and Table 1). Trx is a typical globular molecule, but the axial ratio was calculated to be 3.9 (Fig. 7*F* and Table 1), which is obviously overestimated. It has been reported that the axial ratio of the ORF1p trimer is 13 from sedimentation velocity data but ~3.4 by direct visualization using AFM (48). From the above it seems that the calculated values of the axial ratio from sedimentation velocity data are generally bigger than expected.

Hydrodynamic asymmetry can arise for a variety of reasons other than literal deviations from a spherical shape (48). A configuration with a large surface area and increased subunit flexibility would be expected to increase the frictional coefficient and decrease the sedimentation coefficient (49). For PDI, the multidomain structure, the inter-domain linkers, and the flexible *c* extension may all influence the determinations of the sedimentation and frictional coefficients. As the hydrodynamic calculation from sedimentation velocity data only reflects the maximum shape asymmetry (50), one must be very wary of building a molecular model simply according to the sedimentation velocity data. As a matter of fact, it has already been claimed in the HELP menu for the SEDNTERP program that "at the outset, it must be realized that these parameters, especially that of *a/b*, are merely descriptors for models and may bear little relevance to the actual molecular structure."

C-terminal 441–491 Sequence Contributes to the Abnormality of Molecular Mass Determination by SEC—The intact PDI and PDI mutants containing the fragment 441–491 all display anomalous SEC behavior. The anomalous SEC behavior of PDI was ascribed to its elongated shape with an axial ratio of 5.7 (19); however, PDI shows a short and roughly elliptical cylinder according to the SAXS determination. Adding the fragment 441–491 to the C terminus of Trx resulted in a chimera with anomalous SEC behavior. Similarly, addition of the 99–140 fragment of Syn to the C terminus of Trx resulted in the same anomalous SEC behavior. The 99–140 fragment of Syn is natively unstructured (42), and the 463–491 fragment of PDI is considered as an extension with no definite secondary or tertiary structure (38). Secondary structure prediction using two different programs (51, 52) showed ~62 and ~83% random coil in the PDI fragment 441–491 and the Syn fragment 99–140, respectively (data not shown). No significant difference in CD spectra was detected between PDI, PDI (1–462), and PDI (1–440) and between Trx, Trx-PDI (441–491), and Trx-Syn (99–140) (data not shown). Syn, a 14-kDa natively unfolded monomer, eluted as a single peak at a position corresponding to an apparent molecular mass of 54 kDa on SEC (53). Human Securin, a 22-kDa natively unfolded monomer, eluted with an apparent molecular mass of 5-fold the calculated value (54). It seems the unfolded structure of peptide fragments may contribute to the abnormality of molecular mass determination by SEC.

The presence of Ca^{2+} in a large excess of PDI did not change the SEC behavior of PDI only with a tiny shoulder before the main peak, and this shoulder disappeared when EDTA was also present (data not shown). These results showed that the Ca^{2+} binding does not affect the anomalous chromatographic behavior of PDI.

Acknowledgments—We sincerely thank Prof. K. Kivirikko, University of Oulu, Finland, for the generous gift of the cloned human PDI gene. We thank the following for the helpful suggestions and advice on analytical ultracentrifugation: Dr. J. Lebowitz, Molecular Interactions Resource, Division of Bioengineering and Physical Science, National Institutes of Health, Bethesda; Dr. J. Philo, Alliance Protein Laboratories, Thousand Oaks, CA; Dr. P. Schuck, Protein Biophysics Resource, Division of Bioengineering and Physical Science, National Institutes of Health, Bethesda; Dr. P. Wei, State Key Laboratory of Structural Chemistry for Stable and Unstable Species, College of Chemistry, Peking University, China. We are indebted to X. X. Yu for the expert technical assistance on analytical ultracentrifugation and to Dr. S. Perrett for reading the manuscript. The assistance of Dr. K. Katsumi and Prof. Y. Izumi in the SAXS experiments is greatly appreciated. We thank Dr. D. Svergun for the solution scattering data of bovine serum albumin. We are also grateful to Prof. C. L. Tsou for the continuous encouragement in this work.

REFERENCES

1. Freedman, R. B., Klappa, P., and Ruddock, L. W. (2002) *EMBO Rep.* **3,** 136–140
2. Ellgaard, L., and Ruddock, L. W. (2005) *EMBO Rep.* **6,** 28–32
3. Cai, H., Wang, C. C., and Tsou, C. L. (1994) *J. Biol. Chem.* **269,** 24550–24552
4. Puig, A., and Gilbert, H. F. (1994) *J. Biol. Chem.* **269,** 7764–7771
5. Yao, Y., Zhou, Y. C., and Wang, C. C. (1997) *EMBO J.* **16,** 651–658
6. Tsai, B., Rodighiero, C., Lencer, W. I., and Rapoport, T. A. (2001) *Cell* **104,** 937–948
7. McLaughlin, S. H., and Bulleid, N. J. (1998) *Biochem. J.* **331,** 793–800
8. Pihlajaniemi, T., Helaakoski, T., Tasanen, K., Myllyla, R., Huhtala, M.-L., Koivu, J., and Kivirriko, K. I. (1987) *EMBO J.* **6,** 643–649
9. Wetterau, J. R., Combs, K. A., Spinner, S. N., and Joiner, B. J. (1990) *J. Biol. Chem.* **265,** 9801–9807
10. Koivunen, P., Pirneskoski, A., Karvonen, P., Ljung, J., Helaakoski, T., Notbohm, H., and Kivirikko, K. I. (1999) *EMBO J.* **18,** 65–74
11. Edman, J. C., Ellis, L., Blacher, R. W., Roth, R. A., and Rutter, W. J. (1985) *Nature* **317,** 267–270
12. Freedman, R. B., Hirst, T. R., and Tuite, M. F. (1994) *Trends Biochem. Sci.* **19,** 331–336
13. Darby, N. J., Kemmink, J., and Creighton, T. E. (1996) *Biochemistry* **35,** 10517–10528
14. Kemmink, J., Darby, J., Dijkstra, K., Nilges M., and Creighton, T. E. (1997) *Curr. Biol.* **7,** 239–245
15. Kemmink, J., Darby, N. J., Dijkstra, K., Nilges, M., and Creighton, T. E. (1996) *Biochemistry* **35,** 7684–7691
16. Pirneskoski, A., Klappa, P., Lobell, M., Williamson, R. A., Byrne, L., Alanen, H. I., Salo, K. E., Kivirikko, K. I., Freedman, R. B., and Ruddock, L. W. (2004) *J. Biol. Chem.* **279,** 10374–10381
17. Ohba, H., Harano, T., and Omura, T. (1981) *J. Biochem.* (*Tokyo*) **89,** 889–900
18. Tojo, H., Asano, T., Kato, K., Udaka, S., Horiuchi, R., and Kahinuma, A. (1994) *J. Biotechnol.* **33,** 55–62
19. Solovyov, A., and Gilbert, H. F. (2004) *Protein Sci.* **13,** 1902–1907
20. Hawkins, H. C., de Nardi, M., and Freedman, R. B. (1991) *Biochem. J.* **275,** 341–348
21. Darby, N. J., Penka, E., and Vincentelli, R. (1998) *J. Mol. Biol.* **276,** 239–247
22. Sun, X. X., Dai, Y., Liu, H. P., Chen, S. M., and Wang, C. C. (2000) *Biochim. Biophys. Acta* **1481,** 45–54
23. Svergun, D. I., Volkov, V. V., Kozin, M. B., and Stuhrmann, H. B. (1996) *Acta Crystallogr. Sect. A* **52,** 419–426
24. Chacon, P., Moran, F., Diaz, J. F., Pantos, E., and Andreu, J. M. (1998) *Biophys. J.* **74,** 2760–2775
25. Svergun, D. I. (1999) *Biophys. J.* **76,** 2879–2886
26. Svergun, D. I., Petoukhov, M. V., and Koch, M. H. J. (2001) *Biophys. J.* **80,** 2946–2953
27. Bradford, M. M. (1976) *Anal. Biochem.* **72,** 248–254
28. Ellman, G. L. (1959) *Arch. Biochem. Biophys.* **82,** 70–77
29. Ueki, T., Hiragi, Y., Kataoka, M., Inoko, Y., Amemiya, Y., Izumi, Y., Tagawa, H., and Muroga, Y. (1985) *Biophys. Chem.* **23,** 115–124
30. Guinier, A. G., and Fournet, G. (1955) *Small Angle Scattering X-rays*, pp. 24–28 and 126–133, John Wiley & Sons, Inc., New York
31. Porod, G. (1982) in *Small Angle X-ray Scattering* (Glatter, O., and Kratky, O., eds) pp. 17–51, Academic Press, London
32. Izumi, Y., Kuwamoto, S., Jinbo, Y., and Yoshino, H. (2001) *FEBS Lett.* **495,** 126–130
33. Schuck, P. (2000) *Biophys. J.* **78,** 1606–1619
34. Kemmink, J., Dijkstra, K., Mariani, M., Scheek, R. M., Penka, E., Nilges, M., and Darby, N. J. (1999) *J. Biomol. NMR* **13,** 357–368
35. Kozin, M. B., and Svergun, D. I. (2001) *J. Appl. Crystallogr.* **34,** 33–41
36. Volkov, V. V., and Svergun, D. I. (2003) *J. Appl. Crystallogr.* **36,** 860–864
37. Keller, D. (1991) *Surf. Sci.* **253,** 353–364
38. Noiva, R. (1999) *Semin. Cell Dev. Biol.* **10,** 481–493
39. Puig, A., Primm, T. P., Surendran, R., Lee, J. C., Ballard, K. D., Orkiszewski, R. S., Makarov, V., and Gilbert, H. F. (1997) *J. Biol. Chem.* **272,** 32988–32994
40. Choi, J. Y., Sung, Y. M., Park, H. J., Hur, E. H., Lee, S. J., Hahn, C., Min, B. R., Kim, I. K., Kang, S., and Rhim, H. (2002) *Biotechnol. Appl. Biochem.* **36,** 33–40
41. Nielsen, M. S., Vorum, H., Lindersson, E., and Jensen, P. H. (2001) *J. Biol. Chem.* **276,** 22680–22684
42. Chandra, S., Chen, X., Rizo, J., Jahn, R., and Sudhof, T. C. (2003) *J. Biol. Chem.* **278,** 15313–15318
43. Pirneskoski, A., Ruddock, L. W., Klappa, P., Freedman, R. B., Kivirikko, K. I., and Koivunen, P. (2001) *J. Biol. Chem.* **276,** 11287–11293
44. Koivunen, P., Salo, K. E., Myllyharju, J., and Ruddock, L. W. (2005) *J. Biol. Chem.* **280,** 5227–5235
45. Klappa, P., Ruddock, L. W., Darby, N. J., and Freedman, R. B. (1998) *EMBO J.* **17,** 927–935
46. Darby, N. J., and Creighton, T. E. (1995) *Biochemistry* **34,** 11725–11735
47. McCarthy, A. A., Haebel, P. W., Torronen, A., Rybin, V., Baker, E. N., and Metcalf, P. (2000) *Nat. Struct. Biol.* **7,** 196–199
48. Martin, S. L., Branciforte, D., Keller, D., and Bain, D. L. (2003) *Proc. Natl. Acad. Sci. U. S. A.* **100,** 13815–13820
49. Fleming, K. G., Hohl, T. M., Yu, R. C., Muller, S. A., Wolpensinger, B., Engel, A., Engelhardt, H., Brunger, A. T., Sollner, T. H., and Hanson, P. I. (1998) *J. Biol. Chem.* **273,** 15675–15681
50. Lebowitz, J., Lewis, M. S., and Schuck, P. (2002) *Protein Sci.* **11,** 2067–2079
51. Jones, D. T. (1999) *J. Mol. Biol.* **292,** 195–202
52. Pan, X. M. (2001) *Proteins* **43,** 256–259
53. Huang, C., Ren, G., Zhou, H., and Wang, C. C. (2005) *Protein Expression Purif.* **42,** 173–177
54. Sanchez-Puig, N., Veprintsev, D. B., and Fersht, A. R. (2005) *Protein Sci.* **14,** 1410–1418